Representative Volume Element Calculations under Constant Stress Triaxiality, Lode Parameter, and Shear Ratio

C. Tekoğlu*

Department of Mechanical Engineering, TOBB University of Economics and Technology, Söğütözü, Ankara, 06560, Turkey

Abstract

Recent experiments showed that the Lode parameter, which distinguishes between axisymmetric and shear dominated stress states, has a profound effect on material ductility, especially at low stress triaxiality (Bao and Wierzbicki, 2004; Barsoum and Faleskog, 2007a). Consequently, the theoretical framework for void growth and coalescence is currently being revisited, which often involves performing representative volume element (RVE) calculations. The present study investigates an RVE composed of a cubic unit cell containing a spherical void at its center. The void cell is subjected to a triaxial stress state with $\Sigma_{11}/\Sigma_{22} = \rho_{11}$, $\Sigma_{33}/\Sigma_{22} = \rho_{33}$, plus an additional shear stress component $\Sigma_{12}/\Sigma_{22} = \rho_{12}$. In the coordinate axes aligned with the edges of the cubic void cell, x_i $(i = 1,\ 2,\ 3)$, the non-dimensional stress ratios $\rho_{11},\ \rho_{33}$, and ρ_{12} can be fully characterized by 3 parameters: the stress triaxiality, T, Lode parameter, L, and shear ratio, S. The aim of this paper is to provide an effective method to keep T, L, and S values constant in the entire course of the loading. The effectiveness of the proposed method is validated through several examples covering a wide range of T, L, and S values; the calculations are performed by using the general purpose finite element software ABAQUS.

Keywords: Finite element method, Ductile fracture, Stress triaxiality, Lode parameter, Shear stress

1. Introduction

Finite element (FE) calculations performed on representative volume elements (RVE's) for ideal materials containing periodically distributed voids have been widely used to investigate the growth and coalescence of voids since the seminal works of Needleman and his co-authors (Koplik and Needleman, 1988; Needleman, 1972). Owing to the periodic distribution of voids, the RVE's for such materials correspond to unit cells containing a void at the center, referred to as void cells in the following. Among many others, Barsoum and Faleskog (2007b, 2011); Benzerga et al. (2012); Keralavarma et al. (2011); Leblond and Mottet (2008);

*Corresponding author. Tel.:+90 312 292 42 29 ; fax:+90 312 292 40 91.
Email address: cihantekoglu@etu.edu.tr; C.Tekoglu@gmail.com (C. Tekoğlu)

Lecarme et al. (2011); Nielsen and Tvergaard (2011); Scheyvaerts et al. (2011); Srivastava and Needleman (2013); Tekoğlu et al. (2012); Tvergaard and Nielsen (2010); Yerra et al. (2010) exemplify void cell calculations performed in recent years in order to shed light on different aspects of microscopic mechanisms inherent in the growth and coalescence of voids.

For an RVE subjected to a general stress state with mesoscopic stresses $\Sigma_{11}/\Sigma_{22} = \rho_{11}$, $\Sigma_{33}/\Sigma_{22} = \rho_{33}$, and $\Sigma_{12}/\Sigma_{22} = \rho_{12}$, the stress ratios ρ_{11}, ρ_{33}, and ρ_{12} can be described by 3 parameters, namely, the stress triaxiality, T, Lode parameter, L, and shear ratio, S, in the coordinate axes aligned with the edges of the RVE, see Section 2. Most of the studies on ductile fracture in the literature focus only on the effect of T on ductility, while taking $L = -1$ and $S = 0$, i.e., uniaxial tension plus a hydrostatic stress state (Benzerga and Leblond, 2010; Pardoen et al., 2010; Pineau and Pardoen, 2007; Tvergaard, 1990). Different strategies on how to keep T constant for $L = -1$ and $S = 0$ are discussed by Lin et al. (2006), on circular cylindrical RVE's that allow using two-dimensional (2D) axisymmetric FE meshes. Recent experiments, however, showed that the Lode parameter has a pronounced effect on material ductility, especially at low stress triaxiality (Bao and Wierzbicki, 2004; Barsoum and Faleskog, 2007a). In the literature, there exists several studies systematically investigating the effects of both T and L (e.g. Barsoum and Faleskog, 2007b, 2011; Gao and Kim, 2006; Zhang et al., 2001), and T and S (e.g. Leblond and Mottet, 2008; Nielsen and Tvergaard, 2011; Scheyvaerts et al., 2011; Tekoğlu et al., 2012), on ductility. However, to the best knowledge of the author of this article, the effects of T, L and S have not yet been simultaneously investigated. More importantly, what is missing in the literature is an easy to implement and computationally efficient method that can be used for performing void cell calculations under constant T, L and S ratios, which this paper is aiming to provide.

The paper is organized as follows. Section 2 presents 3 variants of the proposed method, each being the most effective one for a different range of stress states. The method is validated trough several void cell calculations in Section 3. Section 4 discusses the capabilities of the method, and Section 5 highlights the main conclusions of this study.

2. Method

Figs. A-1 and B-1 show the void cell investigated in this study: a cubic unit cell containing a spherical void at its center. In the undeformed (initial) configuration, the edges of the void cell are aligned along the coordinate axes x_i $(i = 1, 2, 3)$, and the initial edge lengths of the void cell are $2L_{10} = 2L_{20} = 2L_{30}$. The initial volume fraction of the spherical void with radius R_0 is therefore given by $f_0 = (\pi R_0^3)/(6L_{10}L_{20}L_{30})$. The void cell is subjected to a triaxial stress state with $\Sigma_{11}/\Sigma_{22} = \rho_{11}$, $\Sigma_{33}/\Sigma_{22} = \rho_{33}$, plus an additional shear stress component $\Sigma_{12}/\Sigma_{22} = \rho_{12}$. It is worth noting that $\Sigma_{12} \neq 0$ prohibits the use of 2D axisymmetric

meshes. The corresponding principal stresses read

$$\begin{aligned}
\Sigma_{\mathtt{I}} &= \frac{\Sigma_{11}+\Sigma_{22}}{2}+\sqrt{\left(\frac{\Sigma_{11}-\Sigma_{22}}{2}\right)^2+\Sigma_{12}^2},\\
\Sigma_{\mathtt{II}} &= \Sigma_{33},\\
\Sigma_{\mathtt{III}} &= \frac{\Sigma_{11}+\Sigma_{22}}{2}-\sqrt{\left(\frac{\Sigma_{11}-\Sigma_{22}}{2}\right)^2+\Sigma_{12}^2},
\end{aligned} \tag{1}$$

with $\Sigma_{\mathtt{I}} \geq \Sigma_{\mathtt{II}} \geq \Sigma_{\mathtt{III}}$. As mentioned earlier, with respect to the coordinate axes aligned with the edges of the void cell, this stress state can be characterized by three non-dimensional parameters, namely, the stress triaxiality T, the Lode parameter L, and the shear ratio S, defined as

$$\begin{aligned}
T &= \frac{\Sigma_{\mathtt{h}}}{3\ \Sigma_{\mathtt{eq}}},\\
L &= \frac{2\ \Sigma_{\mathtt{II}}-\Sigma_{\mathtt{I}}-\Sigma_{\mathtt{III}}}{\Sigma_{\mathtt{I}}-\Sigma_{\mathtt{III}}},\\
S &= \frac{\sqrt{3}\mid \Sigma_{12}\mid}{\Sigma_{\mathtt{eq}}},\\
\Sigma_{\mathtt{h}} &= \Sigma_{11}+\Sigma_{22}+\Sigma_{33},\\
\Sigma_{\mathtt{eq}} &= \frac{1}{\sqrt{2}}\sqrt{\left(\Sigma_{11}-\Sigma_{22}\right)^2+\left(\Sigma_{11}-\Sigma_{33}\right)^2+\left(\Sigma_{22}-\Sigma_{33}\right)^2+6\ \Sigma_{12}^2},
\end{aligned} \tag{2}$$

where $\Sigma_{\mathtt{h}}$ and $\Sigma_{\mathtt{eq}}$ are respectively the hydrostatic and Von Mises equivalent stresses. Expressed in terms of the stress ratios $\rho_{11},\ \rho_{33}$, and ρ_{12}, the non-dimensional parameters read

$$\begin{aligned}
T &= \frac{\sqrt{2}\ \left(1+\rho_{11}+\rho_{33}\right)\ \mathtt{signum}\Big(\Sigma_{22}\Big)}{3\ \sqrt{\left(1-\rho_{11}\right)^2+\left(1-\rho_{33}\right)^2+\left(\rho_{11}-\rho_{33}\right)^2+6\ \rho_{12}^2}},\\
L &= -\frac{\left(1+\rho_{11}-2\ \rho_{33}\right)\ \mathtt{signum}\Big(\Sigma_{22}\Big)}{\sqrt{\left(1-\rho_{11}\right)^2+4\ \rho_{12}^2}},\quad \mid L\mid \leq 1\\
S &= \frac{\sqrt{6}\mid \rho_{12}\mid}{\sqrt{\left(1-\rho_{11}\right)^2+\left(1-\rho_{33}\right)^2+\left(\rho_{11}-\rho_{33}\right)^2+6\ \rho_{12}^2}}\quad 0\leq S\leq 1.
\end{aligned} \tag{3}$$

It is worth emphasizing that there is no unique way for choosing non-dimensional parameters to express a stress state; other equally valid expressions can also be constructed. T, L, and S, in the form presented in Eqs. (3), are those most often encountered in the literature.

T, L and S values are kept constant by keeping the non-dimensional stress ratios ρ_{11}, ρ_{33}, and ρ_{12} constant. Depending on the values of the stress ratios, the same method can be presented in 3 different forms, each being the most effective one for a different range of ρ_{11}, ρ_{33}, ρ_{12} combinations. The boundary conditions for

all 3 formulations are given in Appendices A and B.

The void cell is meshed by using 8-node linear brick elements (C3D8 elements of the ABAQUS element library, see ABAQUS (2012)). The fundamental theorem of homogenization states that the mesoscopic stress components Σ_{ij} of an RVE are related to the microscopic Cauchy stresses σ_{ij} $(i,j=1,2,3)$ through

$$\Sigma_{ij} = \frac{1}{V}\int_V \sigma_{ij}\ \mathtt{d}V, \tag{4}$$

with V being the volume of the RVE, see H. J., Böhm (2012) and references therein. Σ_{ij} for the void cell can therefore be calculated by looping over all the elements: $\Sigma_{ij} = \sum_{e=1}^{N}\left(\sum_{q=1}^{p}\sigma_{ij}^{\{q\}}\ v^{\{q\}}\right)^{\{e\}}/V$, where N is the total number of elements, p is the number of integration points in an element ($p=8$ for C3D8 elements), σ_{ij} and v are, respectively, the local stress and local volume values at the corresponding integration point. The mesoscopic strains, E_{ii}, are given by $E_{ii} = \ln(L_i/L_{i0})$, where L_i and L_{i0} are, respectively, the initial and current half edge lengths of the unit cell.

2.1. CASE I: $\rho_{12} = 0$

$\rho_{12} = 0$ corresponds to zero shear stress, i.e. $S = 0$. In this case, it is enough to mesh only 1/8 of the void cell as shown in Fig. A-1. In the course of deformation, all the edges of the void cell remain straight and aligned with the coordinate axes x_i; i.e. the outer surfaces remain plane as in the undeformed configuration. Symmetry boundary conditions are applied to the bottom, back and middle surfaces, see Appendix A. In order to impose the boundary conditions on the remaining surfaces, a dummy node, $\mathtt{M}_1$, which is not a part of the mesh for the void cell, is created. The displacements of the nodes located at the right, top and front surfaces are coupled to (i.e. forced to have the same values as) the corresponding displacements of node $\mathtt{M}_1$: $\mathtt{u}_1$ for the right surface is coupled to $\mathtt{u}_1^{\mathtt{M}_1}$, $\mathtt{u}_2$ for the top surface to $\mathtt{u}_2^{\mathtt{M}_1}$, and $\mathtt{u}_3$ for the front surface to $\mathtt{u}_3^{\mathtt{M}_1}$. By this way, a concentrated (point) force applied to node $\mathtt{M}_1$ is fully transmitted to the unit cell.

For an RVE in equilibrium under the absence of body forces, the mesoscopic stresses Σ_{ij} can be expressed in terms of surface tractions, t_i, as

$$\Sigma_{ij} = \frac{1}{V}\int_S x_i t_j\ \mathtt{d}S \tag{5}$$

where S and x denote respectively the surface of the RVE and the position vectors of material particles on the surface (see Lin et al. (2006) and references therein). Elaborating on Eq. (5), it is possible to express the mesoscopic stresses acting on the void cell as

$$\Sigma_{11} = \frac{F_1}{A^R},\quad A^R = \left(L_{20}+u_2^{\mathtt{M}_1}\right)\left(L_{30}+u_3^{\mathtt{M}_1}\right),$$
$$\Sigma_{22} = \frac{F_2}{A^T},\quad A^T = \left(L_{10}+u_1^{\mathtt{M}_1}\right)\left(L_{30}+u_3^{\mathtt{M}_1}\right),$$

$$\Sigma_{33} = \frac{F_3}{A^B}, \quad A^B = \Big(L_{10} + u_1^{\mathtt{M}_1}\Big)\Big(L_{20} + u_2^{\mathtt{M}_1}\Big), \tag{6}$$

where F_i denote the resultant of all tractions t_i on the corresponding surfaces; A^R, A^T, and A^B respectively the current areas of the right, top and back surfaces, and L_{i0} the initial half edge lengths of the void cell. In order to apply the forces F_i to the void cell, 3 additional dummy nodes, $\mathtt{N}_i$, are created and connected to node $\mathtt{M}_1$ via spring elements (CONN2D2 elements of the ABAQUS element library, see ABAQUS (2012)), as shown in Fig. A-1. Now, the concentrated forces F_i read

$$F_1 = k\Big(u_1^{\mathtt{N}_1} - u_1^{\mathtt{M}_1}\Big), \quad F_2 = k\Big(u_2^{\mathtt{N}_2} - u_2^{\mathtt{M}_1}\Big), \quad F_3 = k\Big(u_3^{\mathtt{N}_3} - u_3^{\mathtt{M}_1}\Big), \tag{7}$$

with k being the spring constant. So as to keep the stress triaxiality T and the Lode parameter L constant, the following 2 equations need to be satisfied at each strain increment

$$\begin{aligned} \rho_{11} = \frac{\Sigma_{11}}{\Sigma_{22}} = const \Rightarrow \Big(u_1^{\mathtt{N}_1} - u_1^{\mathtt{M}_1}\Big) - \rho_{11}\frac{A^R}{A^T}\Big(u_2^{\mathtt{N}_2} - u_2^{\mathtt{M}_1}\Big) = 0, \\ \rho_{33} = \frac{\Sigma_{33}}{\Sigma_{22}} = const \Rightarrow \Big(u_3^{\mathtt{N}_3} - u_3^{\mathtt{M}_1}\Big) - \rho_{33}\frac{A^B}{A^T}\Big(u_2^{\mathtt{N}_2} - u_2^{\mathtt{M}_1}\Big) = 0. \end{aligned} \tag{8}$$

Eqs. (8) contain 5 unknowns, $u_1^{\mathtt{N}_1}$, $u_3^{\mathtt{N}_3}$, $u_1^{\mathtt{M}_1}$, $u_2^{\mathtt{M}_1}$, and $u_3^{\mathtt{M}_1}$, while $u_2^{\mathtt{N}_2}$ is a prescribed quantity. The multi-point constraints given in Eqs. (8) are introduced to ABAQUS by a user defined subroutine (see the MPC subroutine in (ABAQUS, 2012)). At each strain increment, ABAQUS prescribes the value of $u_2^{\mathtt{N}_2}$ and calculates the 5 unknowns of Eqs. (8) iteratively. The calculation ends when $u_2^{\mathtt{N}_2}$ reaches the value $u_2^{\mathtt{N}_2-max}$, which is the user prescribed boundary condition for $u_2^{\mathtt{N}_2}$.

Each term in Eqs. (8) represents the current value of the corresponding quantity; thus, the obtained T and L values are very accurate. Moreover, as the spring constant k does not enter in Eqs. (8), the results are independent of the value of k. However, both k and $u_2^{\mathtt{N}_2-max}$ indirectly affect the calculations through the "increment size", as discussed in detail in Section 4.

2.2. CASE II: $0 < \rho_{12} < 1, \mid \rho_{11} \mid < 1, \mid \rho_{33} \mid < 1$

In this case, besides the 3 forces given in Eqs. (7), a shear force denoted as F_{12} also acts on the void cell. In order to apply F_{12}, 2 additional dummy nodes, $\mathtt{M}_2$ and $\mathtt{N}_4$, are created and connected to each other via a spring element (CONN2D2 elements of the ABAQUS element library, see ABAQUS (2012)), as shown in Fig. B-1. These 4 concentrated forces associated with 4 springs are transmitted to the void cell by coupling the displacements of the nodes located at the outer surfaces to the corresponding displacements of nodes $\mathtt{M}_1$ and $\mathtt{M}_2$: $\mathtt{u}_1$ for the right surface is coupled to $\mathtt{u}_1^{\mathtt{M}_1}$, $\mathtt{u}_1$ for the left surface is coupled to $-\mathtt{u}_1^{\mathtt{M}_1}$, $\mathtt{u}_1$ for the top surface to $\mathtt{u}_1^{\mathtt{M}_2}$, $\mathtt{u}_2$ for the top surface to $\mathtt{u}_2^{\mathtt{M}_1}$, and $\mathtt{u}_3$ for the front surface to $\mathtt{u}_3^{\mathtt{M}_1}$. The details of the boundary conditions are given in Appendix B. Assuming that F_{12} causes only shear stress in the void cell,

the mesoscopic stresses read

$$\Sigma_{11}=\frac{F_1}{2A^R},\quad \Sigma_{22}=\frac{F_2}{A^T},\quad \Sigma_{33}=\frac{F_3}{A^B},\quad \Sigma_{12}=\frac{F_{12}}{A^T}=\frac{k\Big(u_1^{\mathtt{N}_4}-u_1^{\mathtt{M}_2}\Big)}{A^T}, \tag{9}$$

where F_i are exactly as given in Eqs. (7)[1]. Then, the equations that need to be satisfied to keep the stress triaxiality T, Lode parameter L, and shear ratio S constant, take the form

$$\begin{aligned}
\rho_{11} &= \frac{\Sigma_{11}}{\Sigma_{22}}=const\Rightarrow\Big(u_1^{\mathtt{N}_1}-u_1^{\mathtt{M}_1}\Big)-\rho_{11}\frac{2A^R}{A^T}\Big(u_2^{\mathtt{N}_2}-u_2^{\mathtt{M}_1}\Big)=0,\\
\rho_{33} &= \frac{\Sigma_{33}}{\Sigma_{22}}=const\Rightarrow\Big(u_3^{\mathtt{N}_3}-u_3^{\mathtt{M}_1}\Big)-\rho_{33}\frac{A^B}{A^T}\Big(u_2^{\mathtt{N}_2}-u_2^{\mathtt{M}_1}\Big)=0,\\
\rho_{12} &= \frac{\Sigma_{12}}{\Sigma_{22}}=const\Rightarrow\Big(u_1^{\mathtt{N}_4}-u_1^{\mathtt{M}_2}\Big)-\rho_{12}\Big(u_2^{\mathtt{N}_2}-u_2^{\mathtt{M}_1}\Big)=0.
\end{aligned} \tag{10}$$

Note however that, if the edges of the void cell do not remain straight and parallel to the coordinate axes, F_{12} does not only cause shear stress but also contributes to the normal stress Σ_{11}. Therefore, Eqs. (10) provide acceptable accuracy only if the shear strain of the void cell is relatively small. This is obviously a severe limitation that needs to be resolved. The exact values of the stress ratios at the current increment "$\mathtt{d}$" can be expressed as

$$\begin{aligned}
\frac{\Sigma_{11}^{\mathtt{d}}}{\Sigma_{22}^{\mathtt{d}}} &= Q_0^{\mathtt{d}}\frac{F_1^{\mathtt{d}}}{2A^{R-\mathtt{d}}}\frac{A^{T-\mathtt{d}}}{F_2^{\mathtt{d}}}=Q_0^{\mathtt{d}}\frac{A^{T-\mathtt{d}}}{2A^{R-\mathtt{d}}}\frac{F_1^{\mathtt{d}}}{F_2^{\mathtt{d}}}=Q^{\mathtt{d}}\frac{F_1^{\mathtt{d}}}{F_2^{\mathtt{d}}},\\
\frac{\Sigma_{33}^{\mathtt{d}}}{\Sigma_{22}^{\mathtt{d}}} &= R_0^{\mathtt{d}}\frac{F_3^{\mathtt{d}}}{A^{B-\mathtt{d}}}\frac{A^{T-\mathtt{d}}}{F_2^{\mathtt{d}}}=R_0^{\mathtt{d}}\frac{A^{T-\mathtt{d}}}{A^{B-\mathtt{d}}}\frac{F_3^{\mathtt{d}}}{F_2^{\mathtt{d}}}=R^{\mathtt{d}}\frac{F_3^{\mathtt{d}}}{F_2^{\mathtt{d}}},\\
\frac{\Sigma_{12}^{\mathtt{d}}}{\Sigma_{22}^{\mathtt{d}}} &= \frac{F_{12}^{\mathtt{d}}}{F_2^{\mathtt{d}}},
\end{aligned} \tag{11}$$

where $Q^{\mathtt{d}}$ and $R^{\mathtt{d}}$ are two constants that take different values at each increment. It is not possible, however, to determine $Q^{\mathtt{d}}$ and $R^{\mathtt{d}}$ before actually performing the calculation for increment $\mathtt{d}$. Yet, ensuring that the increment size is "small enough" (see Section 4 for a discussion on the increment size), $Q^{\mathtt{d-1}}$ and $R^{\mathtt{d-1}}$ — obtained in the previous increment — can be employed for the current increment $\mathtt{d}$. Now, Eqs. (10) can be written as

$$\begin{aligned}
\rho_{11} &= \frac{\Sigma_{11}}{\Sigma_{22}}=const\Rightarrow\Big(u_1^{\mathtt{N}_1}-u_1^{\mathtt{M}_1}\Big)-\frac{\rho_{11}}{Q^{\mathtt{d-1}}}\Big(u_2^{\mathtt{N}_2}-u_2^{\mathtt{M}_1}\Big)=0,\quad Q^{\mathtt{d-1}}=\frac{\Sigma_{11}^{\mathtt{d-1}}}{\Sigma_{22}^{\mathtt{d-1}}}\frac{F_2^{\mathtt{d-1}}}{F_1^{\mathtt{d-1}}},\\
\rho_{33} &= \frac{\Sigma_{33}}{\Sigma_{22}}=const\Rightarrow\Big(u_3^{\mathtt{N}_3}-u_3^{\mathtt{M}_1}\Big)-\frac{\rho_{33}}{R^{\mathtt{d-1}}}\Big(u_2^{\mathtt{N}_2}-u_2^{\mathtt{M}_1}\Big)=0,\quad R^{\mathtt{d-1}}=\frac{\Sigma_{33}^{\mathtt{d-1}}}{\Sigma_{22}^{\mathtt{d-1}}}\frac{F_2^{\mathtt{d-1}}}{F_3^{\mathtt{d-1}}},\\
\rho_{12} &= \frac{\Sigma_{12}}{\Sigma_{22}}=const\Rightarrow\Big(u_1^{\mathtt{N}_4}-u_1^{\mathtt{M}_2}\Big)-\rho_{12}\Big(u_2^{\mathtt{N}_2}-u_2^{\mathtt{M}_1}\Big)=0.
\end{aligned} \tag{12}$$

Eqs. (12) contain 7 unknowns, $u_1^{\mathtt{N}_1}$, $u_3^{\mathtt{N}_3}$, $u_1^{\mathtt{N}_4}$, $u_1^{\mathtt{M}_1}$, $u_2^{\mathtt{M}_1}$, $u_3^{\mathtt{M}_1}$, and $u_1^{\mathtt{M}_2}$, while $u_2^{\mathtt{N}_2}$ is a prescribed quantity. The multi-point constraints given in Eqs. (12) are introduced to ABAQUS by a user defined subroutine

[1] Unlike in Eqs. (6), in Eqs. (9), $\Sigma_{11}=\dfrac{F_1}{2A^R}$ because the force F_1 acts on both the right and left surfaces of the void cell, and $A^L=A^R$; see Appendix B.

(see the MPC subroutine in (ABAQUS, 2012)). At each strain increment, ABAQUS prescribes the value of $u_2^{\mathtt{N}_2}$ and calculates the 7 unknowns of Eqs. (12) iteratively. The calculation ends when $u_2^{\mathtt{N}_2}$ reaches the value $u_2^{\mathtt{N}_2-max}$, which is the user prescribed boundary condition for $u_2^{\mathtt{N}_2}$. The force ratios $F_2^{\mathtt{d-1}}/F_1^{\mathtt{d-1}}$ and $F_2^{\mathtt{d-1}}/F_3^{\mathtt{d-1}}$ encountered, respectively, in the expressions for $Q^{\mathtt{d-1}}$ and $R^{\mathtt{d-1}}$ are calculated simply by using Eqs. (7) with the displacements calculated in the previous increment, `d-1`. The mesoscopic stresses in the void cell can be calculated by looping over all the elements as explained in the text below Eq. (4). Hence, the stress ratios that enter into the definitions of $Q^{\mathtt{d-1}}$ and $R^{\mathtt{d-1}}$ are given as

$$\frac{\Sigma_{11}^{\mathtt{d-1}}}{\Sigma_{22}^{\mathtt{d-1}}} = \frac{\sum_{e=1}^{N}\left(\sum_{q=1}^{p}\sigma_{11}^{\{q\}}\ v^{\{q\}}\right)^{\{e\}}}{\sum_{e=1}^{N}\left(\sum_{q=1}^{p}\sigma_{22}^{\{q\}}\ v^{\{q\}}\right)^{\{e\}}}\Bigg|^{\mathtt{d-1}}, \qquad \frac{\Sigma_{33}^{\mathtt{d-1}}}{\Sigma_{22}^{\mathtt{d-1}}} = \frac{\sum_{e=1}^{N}\left(\sum_{q=1}^{p}\sigma_{33}^{\{q\}}\ v^{\{q\}}\right)^{\{e\}}}{\sum_{e=1}^{N}\left(\sum_{q=1}^{p}\sigma_{22}^{\{q\}}\ v^{\{q\}}\right)^{\{e\}}}\Bigg|^{\mathtt{d-1}}. \tag{13}$$

In order to perform the summations in Eqs. (13), an ABAQUS user subroutine that can access the results file during an analysis is written (see the URDFL subroutine in ABAQUS (2012)). For the very first increment of a calculation, i.e. for $\mathtt{d}=1$

$$\mathtt{d}=1 \Rightarrow Q^{\mathtt{d-1}} = Q^0 = \frac{A^{T-0}}{2A^{R-0}} = \frac{L_{10}}{L_{20}}, \quad R^{\mathtt{d-1}} = R^0 = \frac{A^{T-0}}{A^{B-0}} = \frac{L_{30}}{L_{20}}. \tag{14}$$

The smaller the increment size the more accurate the results obtained by using Eqs. (12) to (14). The examples solved in Section 3 for a variety of T, L, and S values show that accurate results are obtained in moderate computation times.

2.3. CASE III: $0 < \rho_{12} < 1, \mid \rho_{11} \mid > 1, \mid \rho_{33} \mid > 1$

In this case, $u_2^{\mathtt{N}_2}$ cannot be chosen as the prescribed quantity because it does not increase monotonically. Instead, $u_1^{\mathtt{N}_4}$ should be prescribed. This leads to the following modifications in Eqs. (12)

$$\begin{aligned}
\frac{\rho_{11}}{\rho_{12}} &= \frac{\Sigma_{11}}{\Sigma_{12}} = const \Rightarrow \left(u_1^{\mathtt{N}_1} - u_1^{\mathtt{M}_1}\right) - \frac{\rho_{11}}{\rho_{12}Q^{\mathtt{d-1}}}\left(u_1^{\mathtt{N}_4} - u_1^{\mathtt{M}_2}\right) = 0, \quad Q^{\mathtt{d-1}} = \frac{\Sigma_{11}^{\mathtt{d-1}}}{\Sigma_{12}^{\mathtt{d-1}}}\frac{F_{12}^{\mathtt{d-1}}}{F_1^{\mathtt{d-1}}},\\
\frac{\rho_{33}}{\rho_{12}} &= \frac{\Sigma_{33}}{\Sigma_{12}} = const \Rightarrow \left(u_3^{\mathtt{N}_3} - u_3^{\mathtt{M}_1}\right) - \frac{\rho_{33}}{\rho_{12}R^{\mathtt{d-1}}}\left(u_1^{\mathtt{N}_4} - u_1^{\mathtt{M}_2}\right) = 0, \quad R^{\mathtt{d-1}} = \frac{\Sigma_{33}^{\mathtt{d-1}}}{\Sigma_{12}^{\mathtt{d-1}}}\frac{F_{12}^{\mathtt{d-1}}}{F_3^{\mathtt{d-1}}},\\
\frac{1}{\rho_{12}} &= \frac{\Sigma_{22}}{\Sigma_{12}} = const \Rightarrow \left(u_2^{\mathtt{N}_2} - u_2^{\mathtt{M}_1}\right) - \frac{1}{\rho_{12}}\left(u_1^{\mathtt{N}_4} - u_1^{\mathtt{M}_2}\right) = 0.
\end{aligned} \tag{15}$$

The force ratios $F_{12}^{\mathtt{d-1}}/F_1^{\mathtt{d-1}}$ and $F_{12}^{\mathtt{d-1}}/F_3^{\mathtt{d-1}}$ encountered, respectively, in the expressions for $Q^{\mathtt{d-1}}$ and $R^{\mathtt{d-1}}$ are calculated simply by using Eqs. (7) with the displacements calculated in the previous increment, `d-1`. Similar to Eqs. (13), the stress ratios are expressed as

$$\frac{\Sigma_{11}^{\mathtt{d-1}}}{\Sigma_{12}^{\mathtt{d-1}}} = \frac{\sum_{e=1}^{N}\left(\sum_{q=1}^{p}\sigma_{11}^{\{q\}}\ v^{\{q\}}\right)^{\{e\}}}{\sum_{e=1}^{N}\left(\sum_{q=1}^{p}\sigma_{12}^{\{q\}}\ v^{\{q\}}\right)^{\{e\}}}\Bigg|^{\mathtt{d-1}},$$

$$\frac{\Sigma_{33}^{\mathtt{d-1}}}{\Sigma_{12}^{\mathtt{d-1}}} = \left. \frac{\sum_{e=1}^{N} \left(\sum_{q=1}^{p} \sigma_{33}^{\{q\}} \; v^{\{q\}} \right)^{\{e\}}}{\sum_{e=1}^{N} \left(\sum_{q=1}^{p} \sigma_{12}^{\{q\}} \; v^{\{q\}} \right)^{\{e\}}} \right|^{\mathtt{d-1}}, \tag{16}$$

$Q^{\mathtt{d-1}}$ and $R^{\mathtt{d-1}}$ for the very first increment d=1 are given by Eqs. (14). The ABAQUS subroutines written for CASE II (MPC and URDFIL, see Section2.3) can be used for CASE III as well after implementing the modifications given in Eqs. (15) and (16). As in CASE II, accurate results are obtained for a variety of T, L, and S values in moderate computation times, see Section 3.

3. Results

The effectiveness of the proposed method is validated through several examples, each with a different T, L, and S combination. An initial porosity of $f_0 = 0.01$ is used for all the examples. The matrix material of the void cell obeys isotropic Hookean elasticity with Young's modulus E and Poisson ratio ν, and the plastic behavior of the matrix is modeled by the rate independent $\mathtt{J}_2$ flow theory. The true stress - true strain behavior for the matrix material is taken to be

$$\begin{aligned} \frac{\sigma}{\sigma_0} &= \frac{E\varepsilon}{\sigma_0} \;\; \mathtt{when} \; \sigma < \sigma_0, \\ \frac{\sigma}{\sigma_0} &= \left(1 + \frac{E\varepsilon_{eq}^{p}}{\sigma_0} \right)^{n} \;\; \mathtt{when} \; \sigma \geq \sigma_0, \end{aligned} \tag{17}$$

where σ_0 is the initial yield stress, ε_{eq}^{p} the equivalent plastic strain, and n the strain hardening exponent. The material properties and the initial porosity has no influence on the effectiveness of the proposed method. Therefore, $E/\sigma_0 = 300$ and $\nu = 0.3$, which are close approximations for a wide range of metallic alloys, are used in this study.

It is worth noting that T and L both depend on the sign of the mesoscopic stress Σ_{22}, see Eqs. (3). Without loss of generality, Σ_{22} is taken to be larger than zero in all the calculations. However, both positive and negative values of T and L are tested, which, in the end, corresponds to altering the sign of Σ_{22}. All the calculations are performed on an "HP Z420" workstation, on 4 central processing units in parallel (cpus=4 in the terminology of ABAQUS, see ABAQUS (2012)).

3.1. CASE I: $\rho_{12} = 0$

For $\rho_{12} = 0$; T, L, and S reduce to

$$T = \frac{\sqrt{2} \left(1 + \rho_{11} + \rho_{33} \right)}{3 \sqrt{\left(1 - \rho_{11} \right)^2 + \left(1 - \rho_{33} \right)^2 + \left(\rho_{11} - \rho_{33} \right)^2}},$$

L	T	ρ_{11}	ρ_{33}	CPU_Time (s)
-1	$\frac{1+2\rho_{11}}{3(1-\rho_{11})}$	$\frac{3T-1}{3T+2}$	ρ_{11}	-
-1	-1	4	4	936.5
-1	0.35	0.0164	0.0164	298.5
-1	1	0.40	0.40	515.6
-1	2	0.625	0.625	380.3
0	$\frac{1+\rho_{11}}{\sqrt{3}(1-\rho_{11})}$	$\frac{\sqrt{3}T-1}{\sqrt{3}T+1}$	$\frac{1+\rho_{11}}{2}$	-
0	1	0.2680	0.6340	757.5
1	$\frac{2+\rho_{11}}{3(1-\rho_{11})}$	$\frac{3T-2}{3T+1}$	1	-
1	1	0.25	1	1045.7

Table 1: Values of the non-dimensional parameters used for CASE I ($\rho_{12} = 0$). The first line for each different L value shows the remaining parameters in a general form, while the following lines show the corresponding values used in the calculations. The last column entitled "CPU_Time" presents the total CPU time in seconds measured by ABAQUS.

$$\begin{aligned} L &= -\frac{\left(1+\rho_{11}-2\,\rho_{33}\right)}{\left(1-\rho_{11}\right)}, \\ S &= 0, \end{aligned} \tag{18}$$

with $\Sigma_{22} > 0$ and $\rho_{11} \neq 1$. Table 1 shows the values of the non-dimensional parameters used in the calculations and the corresponding computation time for each case: for the longest calculation, with $L = T = 1$, the total CPU time (for 4 CPU's) is less than 18 minutes.

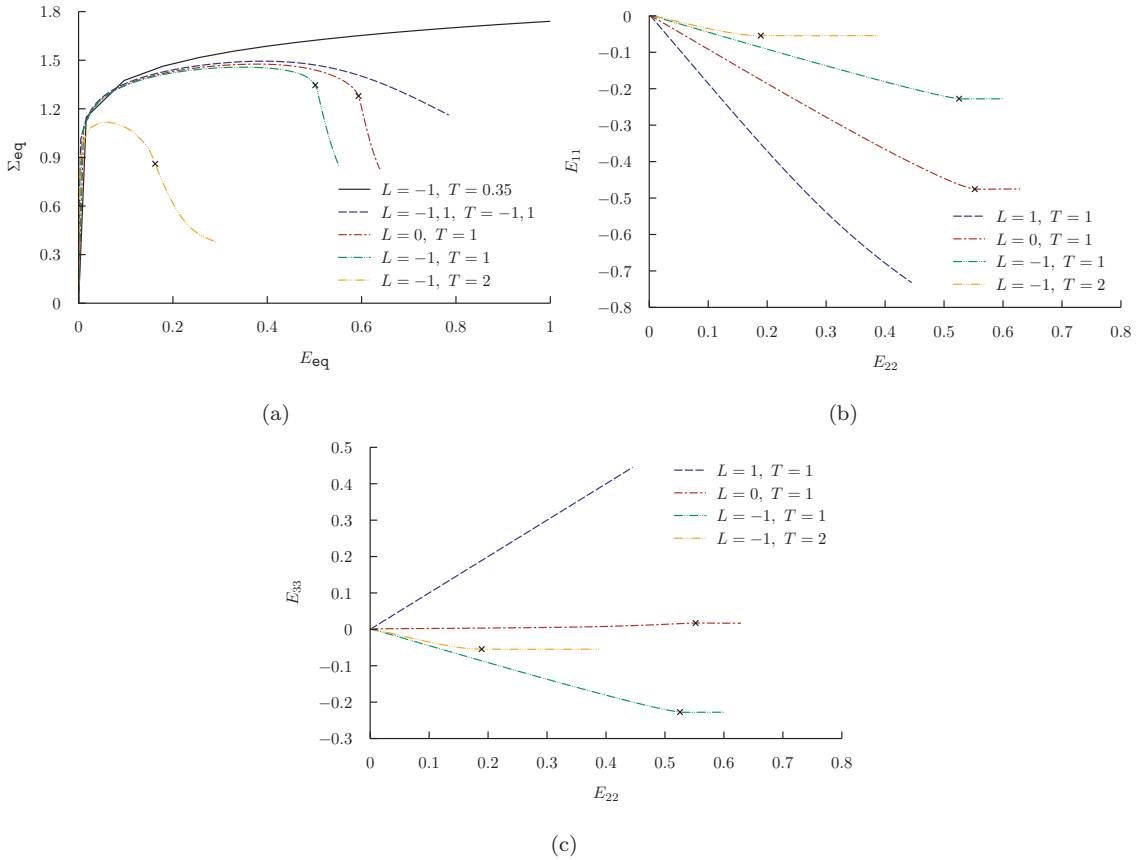

Figure 1: Evolution of: (a) the equivalent stress, Σ_{eq}, with the equivalent strain, E_{eq}, (b) the mesoscopic strain E_{11} with E_{22}, and (c) E_{33} with E_{22}, for the FE calculations introduced in Table 1. The cross signs on curves show the onset of a uniaxial straining mode (with strain rates $\dot{E}_{22} \neq 0;\ \dot{E}_{11} = \dot{E}_{33} = 0$), after which the plastic flow localizes into the ligaments connecting radially adjacent voids, while the regions off the ligaments unload elastically.

For $L = T = -1$, $u_2^{\mathtt{N}_2}$ does not increase monotonically; therefore, either $u_1^{\mathtt{N}_1}$ or $u_3^{\mathtt{N}_3}$ should be used as the prescribed displacement. Employing $u_1^{\mathtt{N}_1}$ leads to the following modifications in Eqs. (8)

$$\begin{aligned} \frac{1}{\rho_{11}} &= \frac{\Sigma_{22}}{\Sigma_{11}} = const \Rightarrow \left(u_2^{\mathtt{N}_2} - u_2^{\mathtt{M}_1}\right) - \frac{1}{\rho_{11}} \frac{A^T}{A^R} \left(u_1^{\mathtt{N}_1} - u_1^{\mathtt{M}_1}\right) = 0, \\ \frac{\rho_{33}}{\rho_{11}} &= \frac{\Sigma_{33}}{\Sigma_{11}} = const \Rightarrow \left(u_3^{\mathtt{N}_3} - u_3^{\mathtt{M}_1}\right) - \frac{\rho_{33}}{\rho_{11}} \frac{A^B}{A^R} \left(u_1^{\mathtt{N}_1} - u_1^{\mathtt{M}_1}\right) = 0, \end{aligned} \tag{19}$$

where all the remaining quantities are as given in Section 2.1.

Fig. 1(a) plots the equivalent stress, Σ_{eq}, versus the equivalent strain, E_{eq}, for the calculations introduced in Table 1. The cross signs on the stress-strain curves show the onset of a uniaxial straining mode (with strain rates $\dot{E}_{22} \neq 0;\ \dot{E}_{11} = \dot{E}_{33} = 0$, see Figs. 1(b) and 1(c)), after which the plastic flow localizes into the ligaments connecting radially adjacent voids, and the regions off the ligaments unload elastically. The onset

of the uniaxial straining mode is a well defined indicator for the onset of void coalescence, and has been widely used in the literature. For $L = -1,\ T = 0.35$ no void coalescence is observed (see also Pardoen and Hutchinson (2000)), and for $L = -1, 1,\ T = -1, 1$, no uniaxial straining mode is observed.

Figs. 2(a) and 2(b) show, respectively, the variation of the percent error in ρ_{11} and ρ_{33} with E_{eq}. The error is calculated by comparing the prescribed ρ_{11} and ρ_{33} ratios with the corresponding values obtained by the FE calculations: $100 \times (\rho_{ii} - \rho_{ii}^{FE})/\rho_{ii},\ i = 1, 3$, no summation on i. For all the cases the error is less than 0.04%, and the maximum error occurs for $L = -1,\ T = 0.35$. In Fig. 2 each strain increment is denoted by a cross sign for $L = -1,\ T = 0.35$. Note that it is possible to obtain more accurate results by decreasing the strain increment size, at the expense of the computation time; see Section 4.

Fig. 3 shows the deformed meshes for the void cells at the onset of the uniaxial straining mode, or, for those cases where a uniaxial straining mode is not observed ($L = -1, 1,\ T = -1, 1$), at the final increment of the calculation. Although a uniaxial straining mode is not observed for $L = -1, 1,\ T = -1, 1$, void sizes and shapes in Figs. 3(c) and 3(d) indicate that void coalescence has already initiated for both cases. That is, if it takes place, the onset of the uniaxial straining mode coincides with the onset of void coalescence. However, depending on T, L, and S values, void coalescence can start with no indication of a uniaxial straining mode. For cases with no uniaxial straining mode, other methods should be used to detect the onset of void coalescence (see e.g. Barsoum and Faleskog (2011)), which is out of scope of the present study.

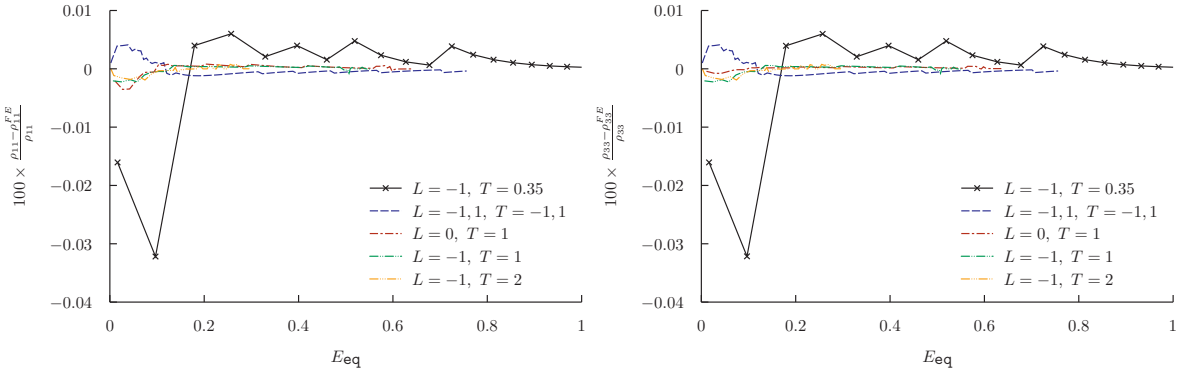

(a) (b)

Figure 2: Variation of the percent error in the stress ratios (a) ρ_{11}, and (b) ρ_{33} with the equivalent strain E_{eq}, for the FE calculations introduced in Table 1. The cross signs on the curve for $L = -1,\ T = 0.35$ indicate the strain increments.

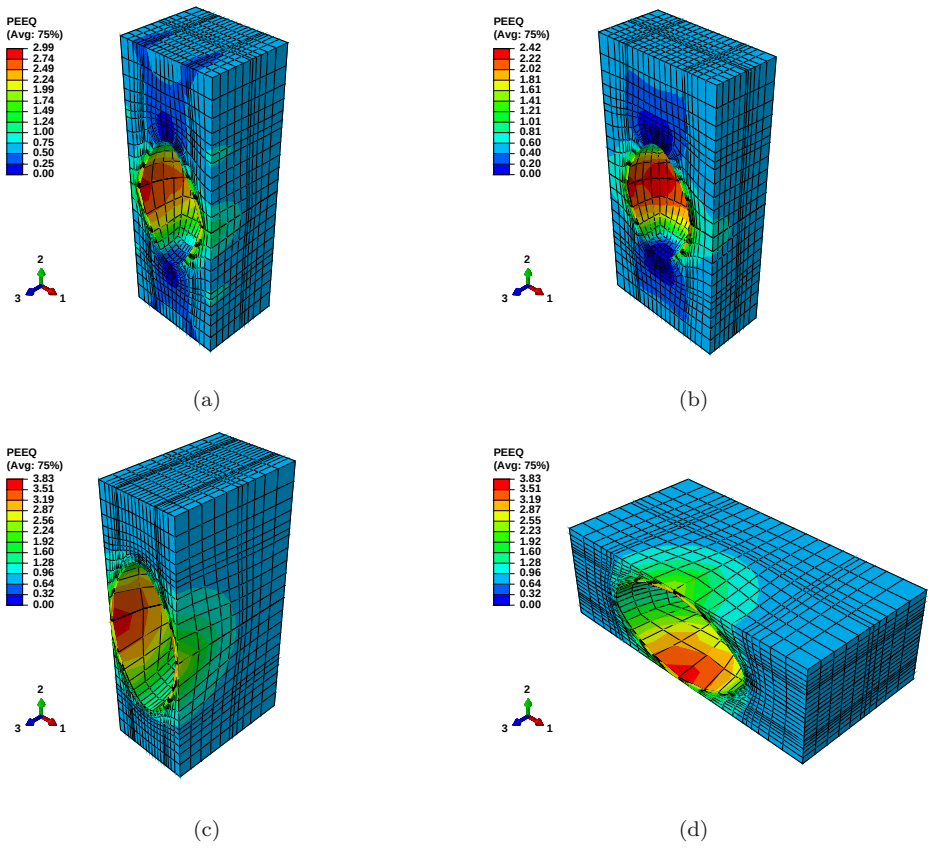

Figure 3: Distribution of the equivalent plastic strain, PEEQ, at the onset of void coalescence for (a) $L = 0,\ T = 1$, (b) $L = -1,\ T = 1$, and at the final increment of the calculation for (c) $L = 1,\ T = 1$, and (d) $L = -1,\ T = -1$. For all the calculations, $S = 0$. Note that only 1/8 of the void cell is meshed for the calculations; the contour plots shown here are obtained by taking the mirror images of the original meshes with respect to the symmetry planes.

3.2. CASE II and CASE III

L	T	S	ρ_{11}	ρ_{33}	ρ_{12}	CPU_Time (s)
-0.99	1	0.1225	0.4027	0.4027	0.0426	1586.3
-0.50	1	0.8321	0.5951	0.5951	0.3507	9825.6
0.00	1	1.0000	1.0000	1.0000	0.5774	1792.6
0.50	1	0.8321	1.8802	1.8802	0.7623	4918.5
0.99	1	0.1225	3.9333	3.9333	0.2090	6963.0
-0.447	1	0.8660	1.6000	1.0000	0.6000	2974.5

Table 2: Values of the non-dimensional parameters used for CASE II (the first two rows) and Case III. The last column entitled "CPU_Time" presents the total CPU time in seconds measured by ABAQUS. For the last calculation (the last row), all three stress ratios, ρ_{ij}, are different, while for the other calculations $\rho_{11} = \rho_{33}$.

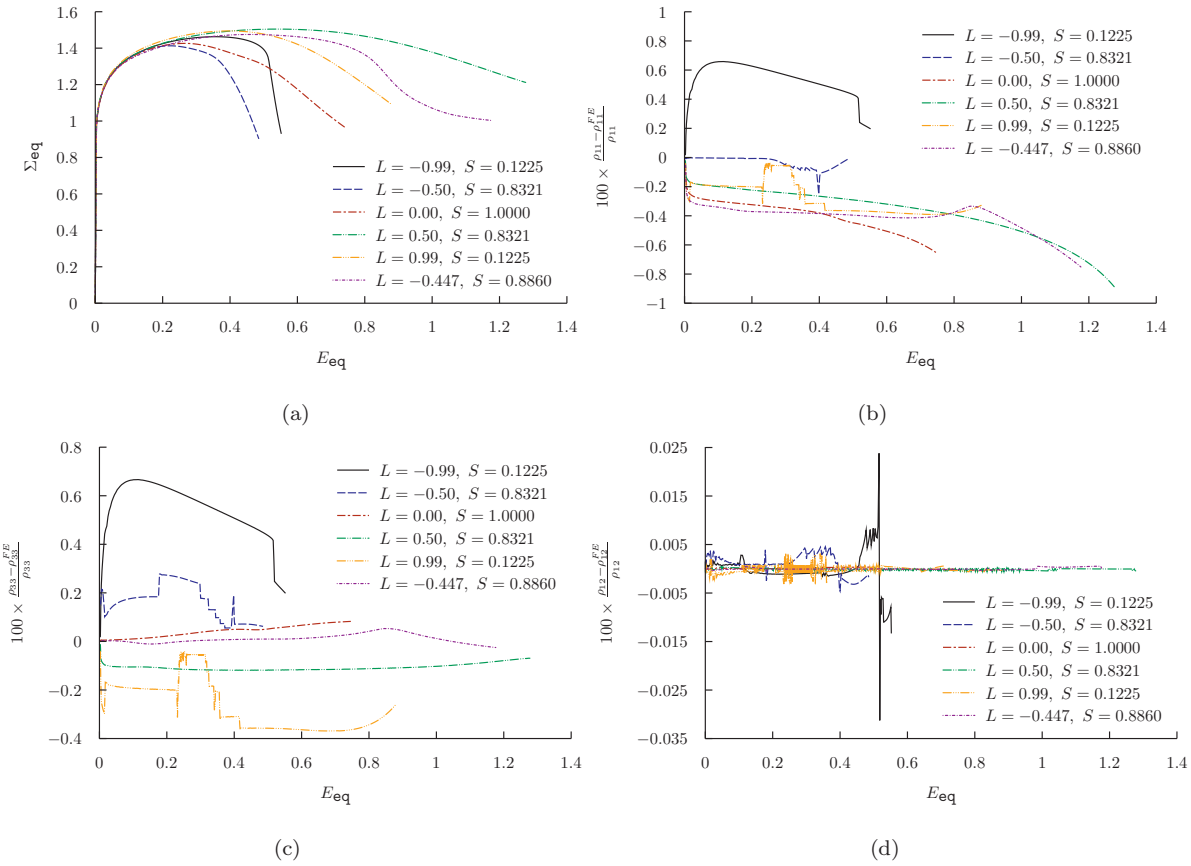

Figure 4: Evolution of the (a) equivalent stress, Σ_{eq}, and the percent error in the stress ratios (b) ρ_{11}, (c) ρ_{33}, and (d) ρ_{12} with the equivalent strain, E_{eq}, for the FE calculations introduced in Table 2. The maximum error occurs for $L = 0.50$, $S = 0.8321$, in ρ_{11}, with an absolute value less than 1%.

Table 2 shows the values of the non-dimensional parameters used in the calculations and the corresponding computation time for each case: for the longest calculation, with $L = -0.5,\ T = 1,\ S = 0.8321$, the total CPU time (for 4 CPU's) is approximately 2 hours and 45 minutes.

For the first 5 calculations introduced in Table 2, where $\rho_{11} = \rho_{33}$, T, L, and S reduce to

$$T = \frac{\left(1 + 2\rho_{11}\right)\ \mathtt{signum}\left(\Sigma_{22}\right)}{3\sqrt{\left(1 - \rho_{11}\right)^2 + 3\rho_{12}^2}},$$

$$L = -\frac{\left(1 - \rho_{11}\right)\ \mathtt{signum}\left(\Sigma_{22}\right)}{\sqrt{\left(1 - \rho_{11}\right)^2 + 4\ \rho_{12}^2}},$$

$$S = \frac{\sqrt{3} \mid \rho_{12} \mid}{\sqrt{\left(1-\rho_{11}\right)^2 + 3\ \rho_{12}^2}}. \tag{20}$$

The inverse relations for Eqs. (20) give the stress ratios as

$$\begin{aligned} \rho_{11} &= \rho_{33} = \frac{3T\sqrt{3+L^2}+2L}{3T\sqrt{3+L^2}-4L}, \\ \rho_{12} &= \frac{3\sqrt{1-L^2}}{3T\sqrt{3+L^2}-4L}, \end{aligned} \tag{21}$$

which are valid for $\mid L \mid \leq 1$, $\Sigma_{22} \neq 0$ and $T \neq 4L/(3\sqrt{3+L^2})$, see also Barsoum and Faleskog (2011). The values of ρ_{11}, ρ_{33}, and ρ_{12} shown in Table 2 are chosen to cover a wide range of different possibilities, and the stress triaxiality is taken to be equal to 1 for all the calculations. For the last calculation (the last row of Table 2), all three stress ratios, ρ_{ij}, are different, while for the other calculations $\rho_{11} = \rho_{33}$.

Fig. 4(a) plots the equivalent stress, Σ_{eq}, versus the equivalent strain, E_{eq}, for the calculations introduced in Table 2. Except for $L = -0.99$, $S = 0.1225$, and $L = -0.50$, $S = 0.8321$, no uniaxial straining mode is observed. However, as can be seen from the deformed meshes of the void cells — at the final increment of the calculation — shown in Fig. 5, all the calculations are continued well beyond the onset of void coalescence. Figs. 4(b) to 4(d) show, respectively, the variation of the percent error in ρ_{11}, ρ_{33}, and ρ_{12} with E_{eq}. The maximum error occurs for $L = 0.50$, $S = 0.8321$, in ρ_{11}, with an absolute value less than 1%.

4. Discussion

In the proposed method, the loading imposed on the void cell is completely controlled by the displacements of the dummy nodes $\mathtt{M}_1$ and $\mathtt{M}_2$; T, L, and S are only internal constraints that define the relative sizes of the components $u_i^{\mathtt{M}_1}$ and $u_i^{\mathtt{M}_2}$. The key idea in this method is that, as the displacements $u_i^{\mathtt{M}_1}$ and $u_i^{\mathtt{M}_2}$ are coupled to (i.e. forced to have the same values as) the corresponding displacements of the surface nodes of the void cell, the forces applied to $\mathtt{M}_1$ and $\mathtt{M}_2$ via spring elements (see Figs. A-1 and B-1) are balanced by the stresses that develop in the void cell. Therefore, the stress ratios ρ_{11}, ρ_{33}, and ρ_{12} can be expressed in terms of the forces applied to the unit cell, and in the end, these expressions reduce to equations in terms of displacements of the dummy nodes, see Eqs. (8), (12), and (15). It is worth noting that the spring constant, k, disappears from these final equations, i.e. the results are independent of the value of k. The increment size and the convergence rate of the FE calculations, however, are affected by the value k for the reasons discussed below.

ABAQUS solves nonlinear equilibrium equations by using Newton's method. The entire loading "step" is divided into a series of "increments", and equilibrium is iteratively satisfied within each increment, see ABAQUS (2012). Although it is possible to define the increment size directly, the easiest and safest

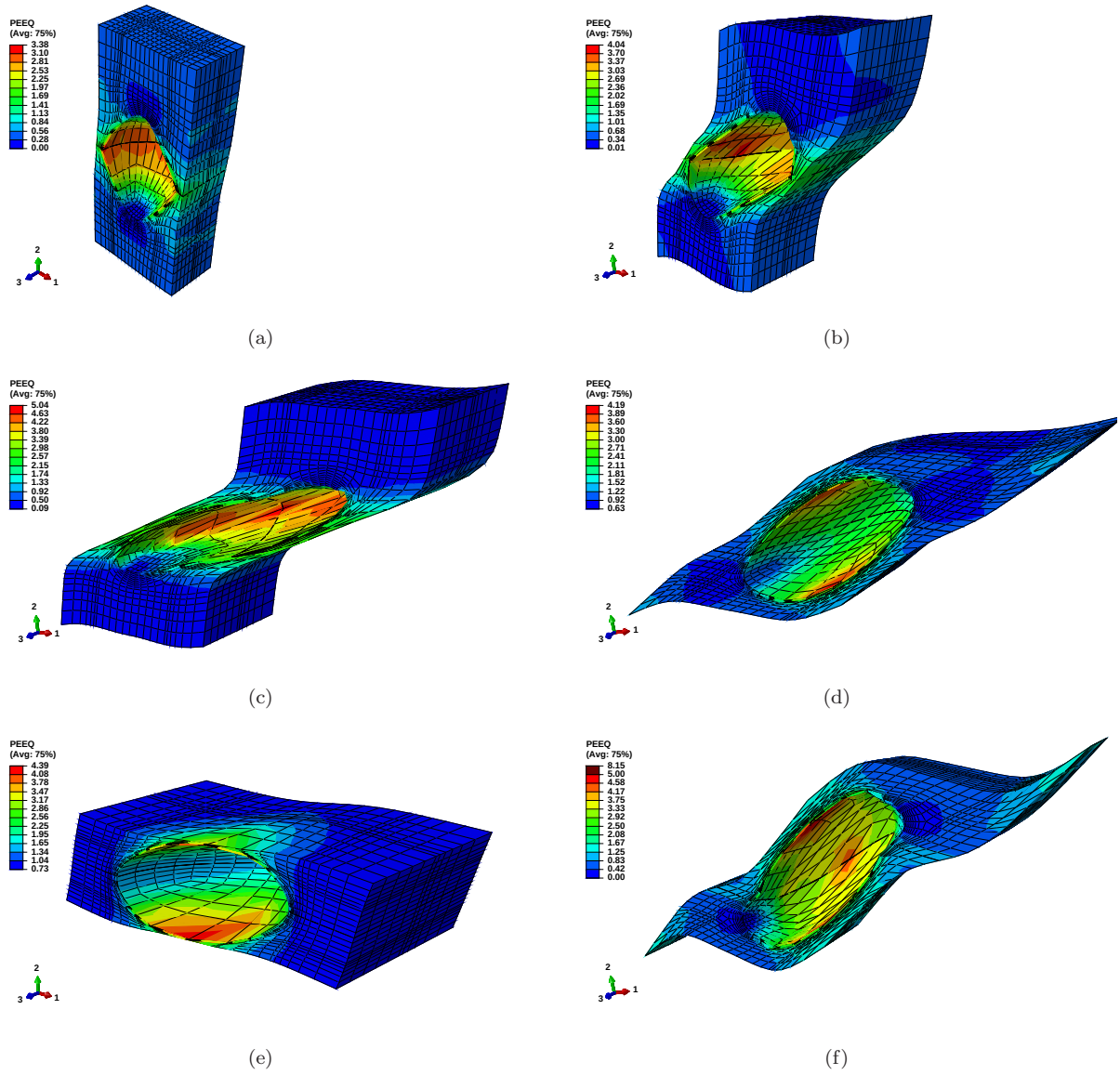

Figure 5: Distribution of the equivalent plastic strain, PEEQ, at the final increment of the calculation for (a) $L = -0.99,\ S = 0.1225$, (b) $L = -0.50,\ S = 0.8321$, (c) $L = 0.00,\ S = 1.0000$, (d) $L = 0.50,\ S = 0.8321$, (e) $L = 0.99,\ S = 0.1225$, (f) $L = -0.447,\ S = 0.886$. For all the calculations $T = 1$; see Table 2 for the other parameters. Note that only 1/4 of the void cell is meshed for the calculations; the contour plots shown here are obtained by taking the mirror images of the original meshes with respect to the symmetry planes.

way is to use automatic incrementation, especially for highly non-linear calculations as discussed in this paper. In automatic incrementation, the user defines 5 parameters: i-) the initial increment size, ii-) the total step size, iii-) the minimum increment size allowed, iv-) the maximum increment size allowed, and v-) the maximum number of increments allowed for the step. The calculation starts with the predefined initial increment size, and if it does not lead to a converged result, it is replaced with a new value within

the limits defined by the user. In the consecutive increments, the increment size is automatically altered by ABAQUS several times by considering both computational efficiency and convergence. If, in an increment, the convergence criteria cannot be satisfied after a number of trials, or if the maximum number of increments allowed for the step is reached, ABAQUS stops the calculation. Both the convergence criteria and the number of trials before a calculation is stopped can be defined by the user, although the default values provided by ABAQUS produce accurate results for a large range of problems (in this paper, the default values are used). The only non-zero degree of freedom prescribed as a boundary condition in the proposed method is $u_2^{\mathtt{N}_2} = u_2^{\mathtt{N}_2-max}$ (or, $u_1^{\mathtt{N}_1} = u_1^{\mathtt{N}_1-max}$, or, $u_1^{\mathtt{N}_4} = u_1^{\mathtt{N}_4-max}$, depending on whether $u_2^{\mathtt{N}_2}$ is a monotonically increasing quantity, see Appendices A and B). For ABAQUS to be able to complete a calculation, i.e. for reaching the condition $u_2^{\mathtt{N}_2} = u_2^{\mathtt{N}_2-max}$, the total step size — which scales with $u_2^{\mathtt{N}_2-max}$ — divided by the average increment size should be less than or equal to the maximum number of increments allowed for the step. Now, if $u_1^{\mathtt{N}_2-max}$ is taken to be a large value, the average increment size should also be large enough to complete the calculation within the limit set for the maximum number of increments. Therefore, for the same limit of the maximum number of increments allowed for a step, a larger $u_2^{\mathtt{N}_2-max}$ value leads to a larger increment size, which may lead to convergence problems. Similarly, employing larger k values leads to larger increment sizes, and therefore to convergence problems: for a large k value, even a small increment in $u_2^{\mathtt{N}_2}$ give rise to a large spring force, which, in turn, leads to large displacements imposed on the void cell in a single increment. For all the calculations presented in this paper, $k = 10^{-1} \times EL_0$ is used, where E is the Young's modulus of the matrix material, and L_0 the half of the initial edge length of the cubic void cell. In order to obtain accurate results while keeping high computational efficiency, an optimum combination of the 5 user defined parameters, convergence criteria, $u_2^{\mathtt{N}_2-max}$, and k values should be employed. Table 3 shows the parameters used for 3 of the calculations presented in Section 3.

ρ_{11}	ρ_{33}	ρ_{12}	$\frac{u_i^{\mathtt{N}_j-max}}{L_0}$	CPU_Time (s)	IIS	TSS	MNIS	MXIS	MNI
0.2500	1	0	5	1045.7	10^{-1}	1	10^{-15}	1	100
0.5951	0.5951	0.3507	5	9825.6	10^{-1}	1	10^{-15}	1	300
3.9333	3.9333	0.2090	5	6963.0	10^{-4}	1	10^{-15}	10^{-4}	650

Table 3: Values of the parameters used for 3 of the calculations presented in Section 3. CPU_Time is the total CPU time in seconds measured by ABAQUS, IIS the initial increment size, TSS the total step size, MNIS the minimum increment size allowed, MXIS the maximum increment size allowed, and MNI the maximum number of increments allowed for the step. The first, second, and third rows, respectively, correspond to longest calculation for CASE I, II and III. For the first and second rows $u_i^{\mathtt{N}_j-max} \equiv u_2^{\mathtt{N}_2-max}$, and for the third row $u_i^{\mathtt{N}_j-max} \equiv u_1^{\mathtt{N}_4-max}$.

The application of the proposed method on 2D axisymmetric void cells to keep the stress triaxiality T constant for $L = -1$ and $S = 0$ is demonstrated by Lecarme et al. (2011). The proposed method can also be used for different RVE's, such as unit cells containing particles or both particles and voids, which are often employed for modeling composite materials. If the unit cell contains only particles but no voids, an easier and computationally more efficient method is to directly apply traction boundary conditions (see Section 3.3 in (Lin et al., 2006)). Note, however, that traction boundary conditions cannot be used in softening regimes.

5. Conclusions

A method is proposed for performing RVE calculations under constant stress triaxiality, T, Lode parameter, L, and shear ratio, S, which corresponds to keeping the stress ratios $\Sigma_{11}/\Sigma_{22} = \rho_{11}$, $\Sigma_{33}/\Sigma_{22} = \rho_{33}$, and $\Sigma_{12}/\Sigma_{22} = \rho_{12}$ constant. Through FE calculations on void cells, it is shown that:

- The proposed method is able to produce accurate results while providing high computational efficiency. For all different cases tested in this paper, the maximum error in the stress ratios is less than 1%, and the total CPU time for the longest calculation is approximately 2 hours and 45 minutes (calculations are performed on an "HP Z420" workstation, on 4 central processing units in parallel).
- Depending on the requirements for the problem at hand, the accuracy and computation time can be adjusted by changing the related parameters as explained in Section 4; more accuracy means more computation time.

Acknowledgements

C. Tekoğlu gratefully acknowledges the financial support provided by The Scientific and Technological Research Council of Turkey, TÜBİTAK (Project No: 111M664).

APPENDIX A - Boundary Conditions for CASE I

Fig. A-1 shows the nomenclature used to define different surfaces of the void cell on which the boundary conditions are applied.

Surface-Right

$$u_1(L_1, x_2, x_3) = u_1^{\mathtt{M}_1}$$

Surface-Top

$$u_2(x_1, L_2, x_3) = u_2^{\mathtt{M}_1}$$

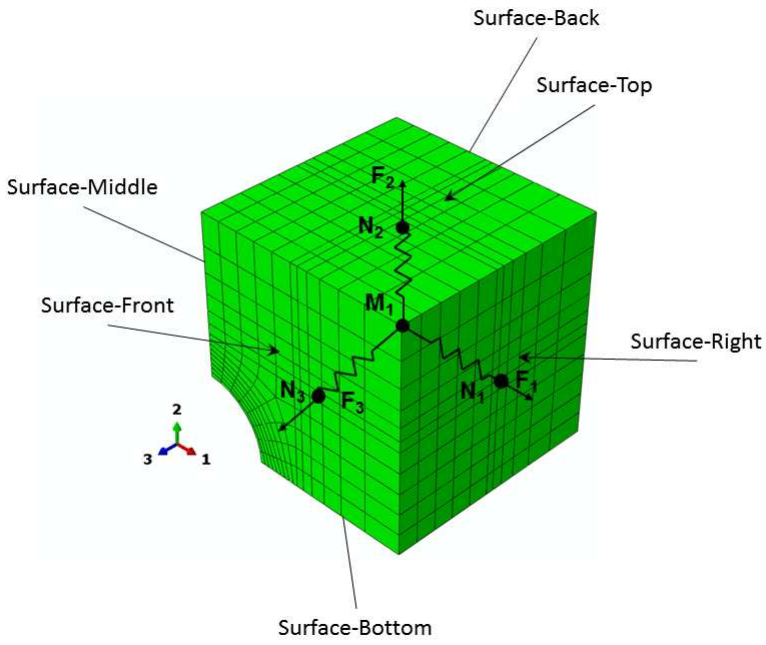

Figure A-1: Finite element mesh for the 1/8 of the void cell with the nomenclature denoting different surfaces on which the boundary conditions are applied. Although the coordinate axes are shown in front of the void cell for visibility, the origin of the reference coordinate system actually corresponds to the point where Surface-Back, Surface-Middle, and Surface-Bottom intersect. For the unit cell shown, the initial porosity is $f_0 = 0.01$. Note that $\mathtt{M}_1$ is a dummy node; the displacements of the nodes located at the right, top and front surfaces of the void cell are coupled to the corresponding displacements of node $\mathtt{M}_1$ so that the concentrated (point) forces applied to node $\mathtt{M}_1$ by the springs are fully transmitted to the unit cell, see Section 2.1

Surface-Front

$$u_3(x_1, x_2, L_3) = u_3^{\mathtt{M}_1}$$

Surface-Middle

$$u_1(0, x_2, x_3) = 0$$

Surface-Bottom

$$u_2(x_1, 0, x_3) = 0$$

Surface-Back

$$u_3(x_1, x_2, 0) = 0$$

In addition to the above equations, if $u_2^{\mathtt{N}_2}$ is a monotonically increasing quantity, $u_2^{\mathtt{N}_2} = u_2^{\mathtt{N}_2 - max}$ should be prescribed as a boundary condition (see Eqs. (8)), otherwise $u_1^{\mathtt{N}_1} = u_1^{\mathtt{N}_1 - max}$ should be prescribed (see Eqs. (19)).

APPENDIX B - Boundary Conditions for CASES II and III

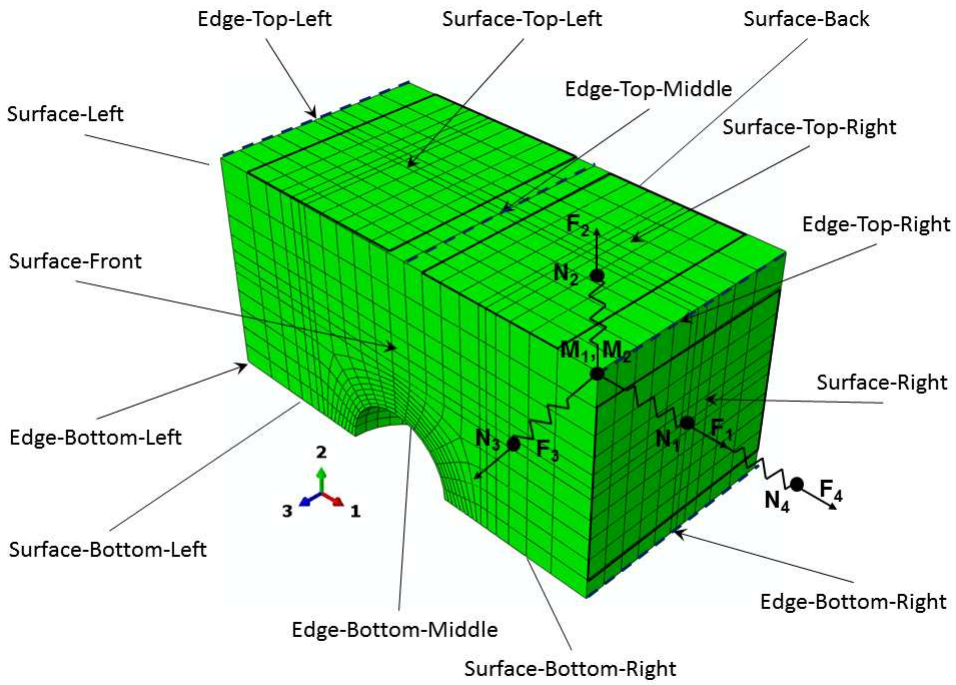

Figure B-1: Finite element mesh for the 1/4 of the void cell with the nomenclature denoting different surfaces and edges on which the boundary conditions are applied. Although the coordinate axes are shown in front of the void cell for visibility, the origin of the reference coordinate system actually corresponds to the point where Edge-Bottom-Middle intersects Surface-Back. For the unit cell shown, the initial porosity is $f_0 = 0.01$. Note that $\mathtt{M}_1$ and $\mathtt{M}_2$ are dummy nodes; the displacements of the nodes located at the left, right, top and front surfaces of the void cell are coupled to the corresponding displacements of node $\mathtt{M}_1$ and $\mathtt{M}_2$ so that the concentrated (point) forces applied to these dummy nodes by the springs are fully transmitted to the unit cell, see Sections 2.2 and 2.3.

Fig. B-1 shows the nomenclature used to define different surfaces and edges of the void cell on which the boundary conditions are applied.

Edge-Top-Middle

$$u_1(0, L_2, x_3) = u_1^{\mathtt{M}_2}$$

$$u_2(0, L_2, x_3) = u_2^{\mathtt{M}_1}$$

Surface-Top-Left/Surface-Top-Right

$$\begin{aligned} u_1(-x_1, L_2, x_3) + u_1(x_1, L_2, x_3) &= 2u_1^{\mathtt{M}_2} \\ u_2(-x_1, L_2, x_3) + u_2(x_1, L_2, x_3) &= 2u_2^{\mathtt{M}_1} \end{aligned}$$

$$u_3(-x_1, L_2, x_3) - u_3(x_1, L_2, x_3) = 0$$

Edge-Top-Left/Edge-Top-Right

$$\begin{aligned} u_1(\pm L_1, L_2, x_3) &= u_1^{\mathtt{M}_2} \pm u_1^{\mathtt{M}_1} \\ u_2(\pm L_1, L_2, x_3) &= u_2^{\mathtt{M}_1} \\ u_3(-L_1, L_2, x_3) - u_3(L_1, L_2, x_3) &= 0 \end{aligned}$$

Surface-Left/Surface-Right

$$\begin{aligned} u_1(-L_1, x_2, x_3) - u_1(L_1, x_2, x_3) &= -2u_1^{\mathtt{M}_1} \\ u_2(-L_1, x_2, x_3) - u_2(L_1, x_2, x_3) &= 0 \\ u_3(-L_1, x_2, x_3) - u_3(L_1, x_2, x_3) &= 0 \end{aligned}$$

Edge-Bottom-Left/Edge-Bottom-Right

$$\begin{aligned} u_1(\pm L_1, 0, x_3) &= \pm u_1^{\mathtt{M}_1} \\ u_2(\pm L_1, 0, x_3) &= 0 \\ u_3(-L_1, 0, x_3) - u_3(L_1, 0, x_3) &= 0 \end{aligned}$$

Edge-Bottom-Middle

$$\begin{aligned} u_1(0, 0, x_3) &= 0 \\ u_2(0, 0, x_3) &= 0 \end{aligned}$$

Surface-Bottom-Left/Surface-Bottom-Right

$$\begin{aligned} u_1(-x_1, 0, x_3) + u_1(x_1, 0, x_3) &= 0 \\ u_2(-x_1, 0, x_3) + u_2(x_1, 0, x_3) &= 0 \\ u_3(-x_1, 0, x_3) - u_3(x_1, 0, x_3) &= 0 \end{aligned}$$

Surface-Back

$$u_3(x_1, x_2, 0) = 0$$

Surface-Front

$$u_3(x_1, x_2, L_3) = u_3^{\mathtt{M}_1}$$

In addition to the above equations, if $u_2^{\mathtt{N}_2}$ is a monotonically increasing quantity, $u_2^{\mathtt{N}_2} = u_2^{\mathtt{N}_2 - max}$ should be prescribed as a boundary condition (see Eqs. (12), CASE II), otherwise $u_1^{\mathtt{N}_4} = u_1^{\mathtt{N}_4 - max}$ should be prescribed (see Eqs. (15), CASE III).

References

ABAQUS, 2012. The Abaqus documentation collection, Version 6.12. Providence, Rhode Island: Dassault Systèmes, (2012).

Bao, Y., Wierzbicki, T., 2004. On fracture locus in the equivalent strain and stress triaxiality space. Int. J. Mech. Sci. 46, 81–98.

Barsoum, I., Faleskog, J., 2007a. Rupture mechanisms in combined tension and shear — Experiments. Int. J. Solids Struct. 44, 1768–1786.

Barsoum, I., Faleskog, J., 2007b. Rupture mechanisms in combined tension and shear — Micromechanics. Int. J. Solids Struct. 44, 5481–5498.

Barsoum, I., Faleskog, J., 2011. Micromechanical analysis on the influence of the Lode parameter on void growth and coalescence. Int. J. Solids Struct. 48, 925 – 938.

Benzerga, A. A., Leblond, J.-B., 2010. Ductile fracture by void growth to coalescence. Adv. Appl. Mech. 44, 169–305.

Benzerga, A. A., Surovik, D., Keralavarma, S. M., 2012. On the path-dependence of the fracture locus in ductile materials analysis. Int. J. Plasticity 37, 157–170.

Gao, X., Kim, J., 2006. Modeling of ductile fracture: Significance of void coalescence. Int. J. Solids Struct. 43, 6277–6293.

H. J., Böhm, 2012. A short introduction to basic aspects of continuum micromechanics. Tech. rep., Institute of Lightweight Design and Structural Biomechanics (ILSB), Vienna University of Technology.

Keralavarma, S. M., Hoelscher, S., Benzerga, A. A., 2011. Void growth and coalescence in anisotropic plastic solids. Int. J. Solids Struct. 48, 1696–1710.

Koplik, J., Needleman, A., 1988. Void growth and coalescence in porous plastic solids. Int. J. Solids Struct. 24, 835–853.

Leblond, J.-B., Mottet, G., 2008. A theoretical approach of strain localization within thin planar bands in porous ductile materials. C. R. Mecanique 336, 176–189.

Lecarme, L., Tekoğlu, C., Pardoen, T., 2011. Void growth and coalescence in ductile solids with stage III and stage IV strain hardening. Int. J. Plasticity 27, 1203–1223.

Lin, R. C., Steglich, D., Brocks, W., Betten, J., 2006. Performing RVE calculations under constant stress triaxiality for monotonous and cyclic loading. Int. J. Numer. Meth. Engng 66, 1331–1360.

Needleman, A., 1972. Void growth in an elastic-plastic medium. J. Appl. Mech. 39, 964–970.

Nielsen, K. L., Tvergaard, V., 2011. Failure by void coalescence in metallic materials containing primary and secondary voids subject to intense shearing. Int. J. Solids Struct. 48, 1255–1267.

Pardoen, T., Hutchinson, J. W., 2000. An extended model for void growth and coalescence. J. Mech. Phys. Solids 48, 2467–2512.

Pardoen, T., Scheyvaerts, F., Simar, A., Tekoğlu, C., Onck, P. R., 2010. Multiscale modeling of ductile failure in metallic alloys. C.R. Phys. 11, 326–345.

Pineau, A., Pardoen, T., 2007. Failure mechanisms of metals. Vol. 2. Elsevier, (Chapter 6).

Scheyvaerts, F., Onck, P. R., Tekoğlu, C., Pardoen, T., 2011. The growth and coalescence of ellipsoidal voids in plane strain under combined shear and tension. J. Mech. Phys. Solids 59, 373–397.

Srivastava, A., Needleman, A., 2013. Void growth versus void collapse in a creeping single crystal. J. Mech. Phys. Solids 61, 1169–1184.

Tekoğlu, C., Leblond, J.-B., Pardoen, T., 2012. A criterion for the onset of void coalescence under combined tension and shear. J. Mech. Phys. Solids 60, 1363–1381.

Tvergaard, V., 1990. Material failure by void growth to coalescence. Adv. Appl. Mech. 27, 83–151.

Tvergaard, V., Nielsen, K. L., 2010. Relations between a micro-mechanical model and a damage model for ductile failure in shear. J. Mech. Phys. Solids 58, 1243–1252.

Yerra, S. K., Tekoğlu, C., Scheyvaerts, F., Delannay, L., Houtte, P. V., Pardoen, T., 2010. Void growth and coalescence in single crystals. Int. J. Solids Struct. 47, 1016–1029.

Zhang, K., Bai, J., Franois, D., 2001. Numerical analysis of the influence of the Lode parameter on void growth. Int. J. Solids Struct. 38, 5847–5856.

Figure captions and Tables

List of Figures

List of Tables